

**X-RAY SYNCHROTRON EMITTING FE-RICH EJECTA IN  
SNR RCW 86**

Jeonghee Rho

SIRTF Science Center, California Institute of Technology, Pasadena, CA 91125

`rho@ipac.caltech.edu`

Kristy K. Dyer

National Radio Astronomy Observatory, Socorro, NM 87801

`kdyer@nrao.edu`

Kazimierz J. Borkowski and Stephen P. Reynolds

Department of Physics, North Carolina State University, Raleigh, NC 27695

`Stephen_Reynolds@ncsu.edu`, `kborkow@unity.ncsu.edu`

Received \_\_\_\_\_; accepted \_\_\_\_\_

## ABSTRACT

Supernova remnants may exhibit both thermal and nonthermal X-ray emission. In a previous study with ASCA data, we found that the middle-aged supernova remnant RCW 86 showed evidence for both processes, and predicted that observations with much higher spatial resolution would distinguish harder X-rays, which we proposed were primarily synchrotron emission, from softer, thermal X-rays. Here we describe *Chandra* observations which amply confirm our predictions. Striking differences in the morphology of X-rays below 1 keV and above 2 keV point to a different physical origin. Hard X-ray emission is correlated fairly well with the edges of regions of radio emission, suggesting that these are the locations of shock waves at which both short-lived X-ray emitting electrons, and longer-lived radio-emitting electrons, are accelerated. Soft X-rays are spatially well-correlated with optical emission from nonradiative shocks, which are almost certainly portions of the outer blast wave. These soft X-rays are well fit with simple thermal plane-shock models. Harder X-rays show Fe  $K\alpha$  emission and are well described with a similar soft thermal component, but a much stronger synchrotron continuum dominating above 2 keV, and a strong Fe  $K\alpha$  line. Quantitative analysis of this line and the surrounding continuum shows that it cannot be produced by thermal emission from a cosmic-abundance plasma; the ionization time is too short, as shown both by the low centroid energy (6.4 keV) and the absence of oxygen lines below 1 keV. Instead, a model of a plane shock into Fe-rich ejecta, with a synchrotron continuum, provides a natural explanation. This requires that reverse shocks into ejecta be accelerating electrons to energies of order 50 TeV. We show that maximum energies of this order can be produced by radiation-limited diffusive shock acceleration at the reverse shocks. In an Appendix, we demonstrate that an explanation of the continuum as due to

nonthermal bremsstrahlung is unlikely.

*Subject headings:* ISM: individual (RCW 86) – supernova remnants – X-rays:  
ISM

## 1. NONTHERMAL X-RAYS AND RCW 86

While most shell supernova remnants (SNRs) show thermal X-ray spectra dominated by emission lines of highly ionized species of C, N, O, Ne, Mg, Si, S, and Fe, a few show featureless spectra which can be well understood as synchrotron emission: SN 1006 (Koyama et al. 1995; Dyer et al. 2001); G347.3-05 (Koyama et al. 1997; Slane et al. 1999), G266.2-1.2 (Slane et al. 2001), and G28.6-0.1 (Bamba et al. 2001). The absence of lines means that a synchrotron interpretation is almost unavoidable; impossibly low abundances and/or peculiar physical conditions would be required to suppress lines completely in a thermal plasma (e. g., Hamilton, Sarazin, & Szymkowiak 1986; Laming 1998), while nonthermal bremsstrahlung implies the presence of electrons that should excite lines as well, and inverse-Compton scattering of any photon population would result in far too hard a spectrum. If synchrotron emission can dominate the spatially-integrated X-ray spectrum of a few remnants, it is likely to play some role in many more, e. g., by totally dominating thermal emission in selected locations within them, or by overwhelming thermal continua (but not lines) in thermally-emitting regions. The signature of an X-ray spectrum with both thermal and synchrotron radiation would be unusually weak lines, diluted by the synchrotron continuum. We interpreted weak X-ray lines in the remnant RCW 86 by such combination of thermal and synchrotron emission, based on ASCA observations (Borkowski et al. 2001, hereafter BRRD). A very similar interpretation of RCW 86 spectra was also proposed by Bamba, Koyama, & Tomida (2000), based on the ASCA Performance Verification data.

RCW 86 (G315.4–2.3) is a large (42′ in diameter) shell-like SNR with a moderate blast wave speed in the range of 400–900 km s<sup>−1</sup>, determined from observations of Balmer-dominated shocks which almost completely encircle the remnant (Long & Blair 1990; Smith 1997; Ghavamian et al. 2001). At a kinematic distance of 3 kpc, its large size and the moderate blast wave speed imply a mature ( $\sim 10^4$  yr old) remnant (Rosado et al. 1996). The bright complex of optical emission filaments at its SW corner, to which the optical designation “RCW86” actually refers, has been generally interpreted as a region where the blast wave impacted a dense ( $\sim 10$  cm<sup>−3</sup>) interstellar cloud. This is also where X-ray and radio emission are the brightest. Radio observations by the MOST telescope at 843 MHz (Whiteoak & Green 1996), with an angular resolution of about 45″, and by the Australia Telescope Compact Array (ATCA) at 1.3 GHz (Dickel et al. 2001), with 8″ resolution, show a complete shell of varying brightness. The radio morphology in the SW region of the remnant is somewhat unusual, consisting of a bright ridge of emission mostly interior to optical and soft X-ray filaments which mark the location of the blast wave. ASCA Performance Verification X-ray spectra showed strikingly weak X-ray lines, much weaker than expected from a normal (solar) abundance plasma, with the exception of the Fe K $\alpha$  line at 6.4 keV (Vink et al. 1997). These results were confirmed by deeper ASCA observations (BRRD) and by more recent BeppoSax observations (Bocchino et al. 2000). A substantial Fe K $\alpha$  equivalent width in the SW suggests enhanced Fe abundance with respect to solar, irrespective of the origin of the underlying high-energy continuum, which led Bocchino et al. (2000) to consider a possibility that we are observing metal-enriched supernova (SN) ejecta.

In our earlier work (BRRD), we used long ASCA observations to deduce the presence of three spectral components: a soft thermal component ( $kT \sim 0.8$  keV), with a relatively long ionization timescale ( $\tau \equiv n_e t \sim 2 \times 10^{11}$  s cm<sup>−3</sup>) and with approximately solar abundances, modeled as a plane shock (XSPEC model *pshock*); a synchrotron component, modeled as

the high-energy tail of the radio spectrum with XSPEC model *srcut*; and a hot thermal component ( $kT \sim 5$  keV,  $\tau \sim 5 \times 10^8$  s cm<sup>-3</sup>) required to account for Fe K $\alpha$  emission. These components varied in relative strength in three regions in the southwest corner of RCW 86. The *srcut* model is just the synchrotron emissivity of a power-law electron distribution with an exponential cutoff, calculated numerically (Reynolds & Keohane 1999); it is characterized by a single free parameter, the peak frequency  $\nu_{\text{rolloff}}$  radiated by electrons with the  $e$ -folding energy of the exponential cutoff. The fitted values of  $\nu_{\text{rolloff}}$  varied from 1 to  $4 \times 10^{16}$  Hz, implying (for  $B \sim 10$   $\mu$ G) maximum electron energies of order 20 TeV. The synchrotron fitting used as inputs the radio fluxes for each region measured from the MOST image (Whiteoak & Green 1996), and an assumed constant spectral index of 0.6.

This analysis explained the ASCA data reasonably well, but with ASCA's spatial resolution of several arcminutes, we were unable to perform several more rigorous tests of the hypothesis of synchrotron X-ray emission. Our spectral fits suggested that the soft thermal emission is due to nonradiative shocks as identified by H $\alpha$  emission, while the synchrotron X-rays should show a spatial distribution similar to radio emission. In an attempt to verify these predictions, we observed RCW 86 with the *Chandra* X-ray Observatory in February 2001. We report here on these observations, which not only confirm our predictions, but allow us to associate synchrotron X-ray emission with Fe-rich SN ejecta seen through Fe K $\alpha$  line emission, and identify all high-energy continuum as synchrotron emission.

## 2. CHANDRA OBSERVATIONS

RCW 86 was observed for 92 ks February 1-2, 2001 (observation id 500170) by the *Chandra X-ray Observatory* (Weisskopf, O'Dell, & van Speybroeck 1996) Advanced CCD Imaging Spectrometer (ACIS: Garmire et al. 1992). Chips I2, I3, S0, S1, S2 and S3 were used, with the pointing center on S3. The focal-plane temperature was  $-120^\circ$  C. The

observations were corrected for radiation damage (referred to as charge transfer inefficiency, CTI) that took place early in *Chandra's* mission, following the procedure in Townsley et al. (2000) which corrects simultaneously for both position-dependent gain shifts and event grade changes. The data were extracted and processed using the *Chandra* Interactive Analysis of Observations software package (CIAO) version 2.1.1. The images were corrected with exposure and instrumental efficiency maps to address chip gaps and mirror vignetting. Instrumental efficiency maps for each chip were created for each energy band (0.5 – 1.0, 1.0 – 2.0, and 2.0 – 8.0 keV), for a single energy in the midrange of each band. The exposure map has been correctly weighted for each chip. The *Chandra* images shown here are binned by a factor of 4 to a resolution of 2"/pixel.

We analyzed extracted spectra with XSPEC 11.1.0 (for introduction to XSPEC, see Arnaud 1996<sup>1</sup>). The spectra were grouped by a minimum of 15 counts per bin. We have experimented with the source spectra and background, comparing CTI-corrected spectra, using Pennsylvania State University software tools (Townsley et al. 2000<sup>2</sup>), and non-CTI-corrected spectra, using standard CXC CIAO tools. The CTI-corrected spectra give more accurate centroids of lines such as Mg and Si, resulting in a particularly significant improvement for the front-illuminated chips. The differences are less than 40 eV for the back-illuminated chip, and although this is less than the ACIS back-illuminated spectral resolution of 100 – 150 eV, the CTI correction provides a significant improvement even for this chip.

The issue of background was not straightforward for this observation since the southeast corner of the supernova remnant nearly fills the S3 chip. Using background from an off-source area and from blank-sky files did not change the fit results (see Table 1)

---

<sup>1</sup>Or visit the web site at <http://heasarc.gsfc.nasa.gov>

<sup>2</sup>Available online at <http://www.astro.psu.edu/users/townsley/cti/>

within the errors. This is partially due to the small contribution (less than 0.5%) of the background to the source counts for RCW 86. Since standard blank sky background is not compatible with the CTI-corrected spectra, we have chosen to take background spectra from off-source areas on the same chip. For the front-illuminated I3 chip with more substantial CTI effects, varying CTI corrections for different regions of the chip constrained us to choose for background a part of the same CTI region as used for the signal, rows 641-768. While these regions likely contain source as well as background photons, since they are from the same chip and have been processed identically with the source regions they should not introduce large errors into the source spectra. Residual instrumental background features such as a faint Si  $K\alpha$  line are present in at least one of our background-subtracted spectra, but since they are very weak they do not pose any problems for spectral fitting.

### 3. RESULTS

#### 3.1. Images

Figure 1 shows the image from the I2, I3, and S0–S3 chips of the SW corner of RCW 86, binned to a resolution of  $2''$  and including the full energy range. The extensive filamentary structure is quite striking and persists down to the scale of the resolution. Most of this structure is parallel to the presumed edge of the remnant. However, some filaments can be seen that are almost radial in orientation, and some emission is considerably more diffuse. Compared to the ROSAT HRI image (Bocchino et al. 2000; Dickel et al. 2001), Figure 1 shows emission extending considerably further ahead of the bright X-ray filaments in the S and SW. Some of that emission is bounded by a sharp-edged filament, but some (in the extreme SW corner, for instance), is not.

Figure 2 contrasts the X-rays in soft (0.5 – 1 keV; red) medium (1 – 2 keV, green), and

hard (2 – 8 keV, blue) energy bands. (The soft and hard band images are shown separately in Figures 3 and 4, respectively.) The brightest emission is clearly relatively soft with some even softer emission further from the remnant center. The network of soft filaments is remarkably similar to the  $H\alpha$  image (Fig. 5, Smith 1997). The hard X-rays have a dramatically different morphology, with completely orthogonal filaments in some locations on S3 and more diffuse emission in I3. The brightest region in the hard X-ray band is the somewhat localized knot near the center of the I3 chip. These morphological differences strongly suggest a different origin for the hard X-rays than for the soft and medium bands, a conclusion confirmed by spectral analysis (see below).

Radio and X-ray morphologies are compared in Figure 6, where X-rays below 2 keV are indicated with green, above 2 keV with blue, as in Figure 2, and radio (the Australia Telescope image: Dickel et al. 2001) in red. While neither X-ray band shows a structure closely resembling radio, there are clear correlations between the hard X-rays and radio: hard X-rays often appear at the edges of radio-emitting regions, most strikingly in a N-S filament of hard X-rays with radio extending beyond to the east, in the center of the S3 chip. We have extracted radio and X-ray profiles from the three rectangular regions shown in Fig. 7, where we have averaged over the narrow dimensions of the rectangles. The profiles are compared in Fig. 8. All three regions show that thin X-ray filaments are associated with rises (or drops) in radio emission, including the hard knot in the center of I3. We interpret these as examples of shocks seen mostly edge-on, with the downstream direction the one in which radio emission rises. We shall argue below that these coincidences support a synchrotron origin for the hard X-ray emission.

### 3.2. Spectra

Figure 7 shows extraction regions for the nonradiative Balmer filament, for the entire hard region on the S3 chip, for the synchrotron filaments alone, and for one region on the I3 chip. The spectrum of the nonradiative shock, visible in optical as a bright Balmer filament, is soft (Figure 9), without any measurable emission above 4 keV. In particular, there is no Fe  $K\alpha$  line emission associated with this shock. We modeled its spectrum with plane shock models *pshock* and *vpshock* which are available in XSPEC (these models, described by Borkowski, Lyerly, & Reynolds 2001, are based on updated thermal plasma code of Hamilton & Sarazin 1984a). Because of calibration problems for the ACIS S3 detector at photon energies below 0.5 keV, we ignored data below this photon energy threshold in all our fits.

We also excluded channels with energies from 1.17 keV to 1.31 keV in our fits to the X-ray spectrum of the soft region. This is the spectral region with “missing” Fe-L shell lines (Brickhouse et al. 2000). Modeling of the Fe L-shell complex in the equilibrium-ionization MEKAL and all non-equilibrium ionization (NEI) models in XSPEC is based on calculations by Liedahl et al. (1995), which did not include electron excitations to levels higher than  $n = 5$ . Brickhouse et al. (2000) found that Fe L-shell lines originating at these highly excited levels cannot be neglected in the ASCA spectrum of Capella. In Capella these lines are produced by  $6 \times 10^6$  K (0.5 keV) plasma in collisional ionization equilibrium, and they cluster near 1.2 keV. Because plasma temperatures are similar in Capella and in our soft regions associated with Balmer filaments, we excluded channels near this energy where we expect Fe L-shell lines originating at  $n > 5$  which are missing in the NEI spectral code.

Results of plane shock fits to the soft spectrum are tabulated in Table 1. In the first fit with *wabs* + *pshock* models, relative abundances of heavy elements are fixed at solar values, but their absolute abundance with respect to H and He is allowed to vary. In the second

fit with *wabs* + *vpshock* models, abundances of individual elements are allowed to vary independently with the following exceptions: the C abundance is tied to the N abundance, and Ca and Ni are tied to Fe. The second fit reproduces the data reasonably well (reduced  $\chi^2 = 2.7$ , see Figure 9). Both models underpredict emission at energies below 0.5 keV by up to a factor of 2, which may be either caused by calibration/instrumental problems or by the presence of additional gas with much lower temperatures in the spectral extraction region. Electron temperatures are relatively low, 0.41 – 0.43 keV, shock ionization ages are relatively short,  $(3 - 5) \times 10^{10} \text{ cm}^{-3} \text{ s}$ , and elemental abundances are close to solar. The largest departures from solar abundances occur for Fe and Mg, whose apparent subsolar abundances might be caused by moderate depletion onto dust grains and by overlapping Fe L-shell lines from high  $n$  levels, which are adjacent to the Mg  $K\alpha$  line. An apparent excess of emission near 3 keV hints at the presence of the Ar  $K\alpha$  line (Ar is not included in the NEI code).

There is no evidence for the presence of excess emission at high energies, suggesting that thermal plane shock models with constant electron temperature and approximately solar abundances provide a satisfactory description of the soft spectrum. This finding fully confirms our previous inferences (BRRD) about the thermal nature of the soft X-ray emitting filaments which are associated with the blast wave propagating into the ambient ISM.

We realize that our very simple single plane-shock model for the soft emission is quite unrealistic. In the multiband X-ray image (Figure 2), it is clear that the bright thermal filaments have spectral differences on spatial scales much smaller than the size of our spectral extraction regions, and extending down nearly to the *Chandra* spatial resolution limit. The small values of ionization timescale  $\tau$  we find may be artifacts of using constant-temperature shock models to fit regions with clearly varying temperatures.

The focus of the present investigation is understanding the harder emission, and for that purpose we simply require an adequate description, if not a full explanation, of the soft emission. We defer to a later work a more extensive exploration of the nature of the soft emission and possible explanations for the short ionization timescale.

Spectra of hard regions are shown in Figure 10 (the entire synchrotron-emitting region in the NE corner of the S3 chip) and Figure 11 (synchrotron filaments on S3 and I3 chips). (See Figure 7 for the locations of these regions.) Results of fits with the *srcut* + low-temperature *vpshock* models are shown in these Figures and tabulated in Table 1. The Fe  $K\alpha$  line is modeled by an additional pure Fe *vpshock* model (see § 4.2 for further details). Ideally, one uses the *srcut* model with radio information as input: the 1 GHz radio flux of the region and the spectral index. The integrated spectral index of the entire RCW 86 remnant is about 0.6, based on single-dish observations (typical errors are  $\pm 0.05$ ), but accurate fluxes cannot be determined because the only available radio images are interferometer images, in which the absence of very short antenna baselines means that very smoothly distributed flux is resolved out. In fact, the MOST image at 843 MHz (Whiteoak & Green 1996) contains less than 40% of the single-dish flux at that frequency, while the ATCA image (Dickel et al. 2001) contains about 70% of the 1.3 GHz single-dish flux. In local regions, the total flux can be in error by even larger factors. As a result, we cannot use the measured radio fluxes to constrain the X-ray modeling. Instead, we have fixed the radio spectral index at 0.6 and actually fit for the radio flux. The values we obtain are quite reasonable and within factors of 2 of the fluxes measured from the radio maps (which differ between themselves by a comparable factor).

Nonthermal X-ray emission from RCW 86 was reported from *Rossi* X-ray Timing Explorer (RXTE) observations by Allen et al. (1999). The spatial resolution of RXTE is only about one degree, so it cannot resolve RCW 86. Allen et al. (1999) report that

its spectrum observed with the PCA instrument is well described by a power-law with energy index  $\Gamma = 3.3 \pm 0.2$  between 10 and 24 keV. Our *srcut* model, with parameters fit to the hard region as described above, is slightly curved in that interval, with a mean slope between 10 and 20 keV of  $\Gamma = 3.5$ . It predicts a flux at 10 keV smaller than that quoted by Allen et al. (1999) by a factor of 12.5, and gives a 1 GHz radio flux of 2.59 Jy. If we simply scale up our X-ray model to the flux level reported by Allen et al. (1999) by that factor, the predicted radio flux at 1 GHz is 32 Jy. Green (2001<sup>3</sup>) reports the observed 1 GHz flux of RCW 86 to be 49 Jy. We regard this crude agreement, to within 50% after an extrapolation of nine orders of magnitude in photon frequency, as evidence of broad consistency between the whole-remnant spectrum seen by RXTE and the local spectra we fit in individual synchrotron filaments, consistency which represents strong support for the idea of a substantial synchrotron component in the spectrum of RCW 86.

For the soft thermal regions, we also attempted to bound any nonthermal emission. We obtained a quantitative upper limit on the presence of a synchrotron component by adding to the fit an *srcut* component, with a 1 GHz flux determined from the Australia Telescope observations (Dickel et al. 2001) and assuming a spectral index of 0.6, allowing  $\nu_{\text{rolloff}}$  to vary. The fits rejected values of  $\nu_{\text{rolloff}}$  larger than about  $2 \times 10^{16}$  Hz.

Attempts to fit the hard continuum and the Fe  $K\alpha$  line with pure thermal models are discussed below; we find that the resulting extremely short ionization timescales are inconsistent with the known age of the remnant, which should be the shock age if the Fe  $K\alpha$  line is due to solar abundance Fe from the ISM.

---

<sup>3</sup>Available online at <http://www.mrao.cam.ac.uk/surveys/snrs/>

## 4. DISCUSSION

### 4.1. Morphological Evidence for Synchrotron Emission

We believe that the striking difference in morphology of hard and soft X-rays is strong evidence in favor of the synchrotron interpretation of the bulk of the harder X-ray continuum (above 2 keV). The spectrum of regions bright in X-rays below 2 keV is well described by thermal plane-shock models. The hard X-rays show a dramatically different structure, often occurring on the edges of regions of radio emission. It is sometimes claimed that a nonthermal interpretation of X-rays requires that the X-ray and radio morphologies be identical. This is only true to the extent that synchrotron losses on electrons can be neglected, rarely the case except for very young remnants such as the historical Galactic remnants. In a magnetic field of  $10 \mu\text{Gauss}$ , electrons radiating the peak of their synchrotron emission at  $h\nu = 4 \text{ keV}$  lose half their energy in 900 years, far less than the presumed age of order  $10^4 \text{ yr}$ , while electrons radiating chiefly at 1 GHz will last for over  $10^7 \text{ yr}$ . Thus we should expect synchrotron X-rays to be seen near the shocks where the electrons are presumably accelerated, while radio emission can be seen there as well as far downstream.

In the complex inhomogeneous environment of RCW 86, shock structures can be found in various locations inside the outermost X-ray and radio emission. Some may be parts of the reverse shock or secondary shocks driven into denser clouds, and projection effects further complicate the interpretation. However, a particularly clear example of what appears to be an internal shock seen edge on is indicated in the central (“hard-filament”) extraction region on chip S3 in Figure 7, and profiles along the indicated direction are shown in Figure 8. Here, both radio and X-ray emission appear fairly abruptly; the X-ray emitting region is only a few tens of arcseconds wide, while radio emission persists much further, just as expected if this is an outward facing shock at which electrons are newly accelerated. At a distance of 3 kpc,  $1''$  corresponds to  $0.015 \text{ pc}$  or  $4.5 \times 10^{16} \text{ cm}$ . Shock velocities from

optical or X-ray analysis are of order  $600\text{--}900\text{ km s}^{-1}$ , so that one might expect post-shock flow velocities in the plane of the sky to be of the same order, but somewhat smaller. In 900 years, a flow at  $500\text{ km s}^{-1}$  travels a distance  $l = 0.46\text{ pc}$  corresponding to an angular distance of  $32''$ . This compares reasonably well with the thickness of the overall X-ray emitting peaks in the profiles of Figure 8, allowing for projection effects and effects of magnetic-field geometry, which can account for the irregular shapes of the profiles. In general, we should expect synchrotron-emitting regions to have thicknesses of order a few tens of arcseconds, though if a shock is seen close to face-on, one will obtain more diffuse, fainter extended emission. These properties do appear to characterize the structure of the hard X-ray emission as well as can be expected.

We do not see clear evidence for hard X-ray emission from the extreme outer edge of the X-ray emission seen in the lower part of the S3 chip, where at least one part of the blast wave is presumably encountering undisturbed upstream material. However, the overall faintness of the emission (presumably mostly thermal) is such that a faint nonthermal component might be hard to discern. Unfortunately, the emission there is too faint for useful spectral analysis with these data. Interior shocks could be portions of the outer blast wave encountering denser material and seen in projection, or portions of a reverse shock moving back into the interior from such an encounter. It seems that such interior shocks are where most hard X-rays originate, though not at the  $\text{H}\alpha$ -bright nonradiative shocks which are probably the blast wave moving into partially neutral material. This is an extremely interesting result, as it suggests that electrons may be accelerated at reverse shocks as well as at forward shocks – perhaps preferentially at reverse shocks in RCW 86. In the prototype synchrotron-X-ray-dominated remnant, SN 1006, no obvious reverse-shock structure is seen, and the hardest emission appears to come from closest to the outer remnant edge. While a reverse shock is almost certainly present in SN 1006, one can explain its absence in radio or X-ray nonthermal emission if the magnetic field threading the ejecta is very weak, as

one might expect if it is just the magnetic field of the progenitor, enormously diluted by expansion with flux freezing. The situation appears to be different in RCW 86.

#### 4.2. Spectroscopic Evidence for Fe-rich SN ejecta

The Fe  $K\alpha$  line at 6.4 keV in RCW 86 has been puzzling since Vink et al. (1997) reliably determined its energy, because such a low energy implies the presence of only very low ionization stages of Fe in the X-ray emitting plasma. Vink et al. (1997) suggested strong deviations from a Maxwellian electron distribution in order to account for both the presence of the Fe line and the weakness of other emission lines at low energies. Subsequent studies (BRRD; Bamba, Koyama, & Tomida 2000; Bocchino et al. 2000) have generally postulated its origin in a hot ( $\sim 5$  keV) plasma in the remnant’s interior. A substantial Fe  $K\alpha$  strength suggests that Fe is overabundant by a factor of several with respect to cosmic (solar) abundances, but this finding is somewhat uncertain in view of the poor photon statistics and uncertainties in atomic data. Although our *Chandra* observations of RCW86 also suffer from poor photon statistics at high energies, the high spatial resolution of *Chandra* allows us to spatially separate the synchrotron-emitting regions and the soft thermally-emitting X-ray filaments. We find that Fe  $K\alpha$  is associated with the synchrotron-emitting regions, and not with the thermal filaments. Apparently, fast electrons capable of exciting Fe  $K\alpha$  are present in synchrotron emitting regions, and absent in soft X-ray filaments.

It seems natural to assume that the Fe  $K\alpha$  line is produced in a hot thermal plasma with an approximately cosmic composition, where most free electrons are provided by the ionization of H and He. In this hypothesis the observed high-energy continuum must be thermal, because a substantial contribution from synchrotron emission would demand a high derived Fe abundance for the line to rise above the continuum, and this would be obviously in conflict with the assumed solar composition. This interpretation unexpectedly

encounters a timescale problem which makes it untenable, as we now demonstrate. We use the fitted ionization timescale  $n_e t$ , and derive  $n_e$  from the observed X-ray flux in the model to obtain a characteristic age of the shocked plasma under this assumption.

For a plasma consisting mostly of H and He, we can set a lower limit to the electron density in the synchrotron-emitting region by fitting a thermal NEI model to the high-energy *Chandra* spectrum. But because the *Chandra* spectrum is rather noisy in the vicinity of the Fe K $\alpha$  line, we shall obtain the temperature, Fe abundance, and ionization timescale from high-quality ASCA GIS spectra presented by us previously (BRRD). (The analysis of the Fe K $\alpha$  line in BRRD was influenced by an error in all NEI models in XSPEC v10, which resulted in a missing Fe K $\alpha$  fluorescence line at extremely low ionization timescales relevant for RCW86. This error is not present in the NEI models in XSPEC v11.) The corrected values for the *rnei* model fit to GIS spectra above 5.5 keV are: plasma temperature of 5.0 keV (with a 90% confidence interval of 3.5–7.6 keV), a very low ionization timescale  $\tau$  of  $2.8 \times 10^8 \text{ cm}^{-3} \text{ s}$  (less than  $6.6 \times 10^9 \text{ cm}^{-3} \text{ s}$  with 90% confidence), and an Fe abundance of 1.6 solar (with 90% confidence interval 1.1–2.5). By using these best-fit values, we find that this model must be normalized to 0.0048 (in XSPEC units for thermal models: normalization =  $(10^{-14}/4\pi D^2) \int n^2 dV$ , where  $D$  is the distance to the source in cm and  $n$  is the electron density). This value is required to account for the high energy emission seen in Figure 10, implying an emission measure  $EM = \int n_e n_H dV$  of  $5.2 \times 10^{56} d_3^2 \text{ cm}^{-3}$  (where  $d_3$  is the remnant’s distance in units of 3 kpc). The extraction region is approximately  $2'.4 \times 5'.0$  in size, spanning the entire width of the synchrotron-emitting region. This translates into a surface area of  $2.1 \times 4.2 \text{ pc}^2$  at 3 kpc distance. Assuming 4.2 pc depth, we estimate the volume of the X-ray emitting region to be  $37 d_3^3 \text{ pc}^3$ . For H and He dominated plasma, we then arrive at an electron density  $n_e$  of  $0.76 f^{-1/2} d_3^{-1/2} \text{ cm}^{-3}$ , where  $f$  is the volume filling fraction of the hot gas. The plasma characteristic “age” is then  $\leq \tau/n_e = 12 f^{1/2} d_3^{1/2} \text{ yr}$ , which is far too short compared with the age of the remnant.

The upper limit on  $\tau$  from fits to ASCA GIS data is of course much larger than the best-fit value of  $2.8 \times 10^8 \text{ cm}^{-3} \text{ s}$  used in these estimates, but we can establish a more stringent upper limit on  $\tau$  which applies for plasmas with approximately cosmic composition. We noted previously an extreme sensitivity of NEI models to ionization timescale (Figure 8 in BRRD). At extremely low ionization timescales, most abundant elements such as O have not been stripped of their L-shell electrons, resulting in weak X-ray lines in the *Chandra* ACIS spectral range and low X-ray fluxes at low energies. As the ionization timescale increases, electrons are stripped from their L shells, and the soft X-ray flux increases dramatically. By varying the ionization timescale, we find that the *vnei* model with the temperature and Fe abundance quoted above and  $N_H = 4.2 \times 10^{21} \text{ cm}^{-2}$  (from model B in Table 1) produces strong O lines at low energies which are inconsistent with *Chandra* spectra for  $\tau > 1 \times 10^9 \text{ cm}^{-3} \text{ s}$ . (We obtained this conservative upper limit by requiring that the calculated spectrum not exceed the observed count rate at the location of O lines. But in contrast to observations, O lines are very prominent in strongly-underionized models, so based on consideration of the spectral shape one can probably reject models with  $\tau$  as short as  $5 \times 10^8 \text{ cm}^{-3} \text{ s}$ .) This constraint on ionization timescale gives an age of less than 40 yr. By assuming a much higher plasma temperature we can perhaps push this limit to  $\sim 100$  yr, which is still much less than expected for a relatively old remnant such as RCW 86. This timescale problem is not an entirely new finding, as an inspection of previous results obtained with various satellites demonstrates it clearly, but new constraints from *Chandra* are particularly severe. The Fe  $K\alpha$  line and continuum at high energies cannot be easily produced by a thermal plasma with approximately solar abundances.

A consideration of Coulomb interactions between ions and electrons (see the Appendix) leads us to a conclusion that the observed continuum in regions of the remnant with hard spectra cannot be produced by nonthermal bremsstrahlung in cosmic abundance plasmas. This leaves synchrotron radiation as the preferred explanation for the observed continuum

in the whole *Chandra* spectral range, including high energies. But the Fe  $K\alpha$  line must be produced by collisional excitations and ionizations by much less energetic thermal electrons. Because the Fe  $K\alpha$  line strength relative to the high energy continuum already implies above solar abundances, it is likely that we are observing highly-enriched SN ejecta. SN ejecta were already considered in some detail by Bocchino et al. (2000), but now we have indirect evidence for the presence of very Fe-rich ejecta. For simplicity, we considered pure Fe-rich ejecta and modeled them by the *vpshock* model with temperature 5 keV and ionization timescale  $10^9 \text{ cm}^{-3} \text{ s}$ . These plasma parameters are just rough guesses: at much lower temperatures most thermal electrons are not capable of exciting the Fe  $K\alpha$  line, while at ionization ages above a few  $\times 10^9 \text{ cm}^{-3} \text{ s}$ , Fe L shell emission becomes very prominent (in conflict with *Chandra* observations). In addition to the pure Fe *vpshock* model which accounts for the Fe  $K\alpha$  line, we used the *srcut* model for modeling synchrotron emission. The blast wave seen in projection against synchrotron-dominated regions is modeled by a low-temperature *vpshock* model, either with solar abundances, or with abundances determined from our fit to the spectrum of the Balmer-dominated nonradiative shock. Results are tabulated in Table 1.

The Fe  $K\alpha$  line is unambiguously detected only in the spectrum of the entire synchrotron-emitting region on the NE corner of the S3 chip (see Figure 7). The emission measure  $EM_{Fe} = \int n_e n_{Fe} dV$  of pure Fe-rich ejecta is  $3.1 \times 10^{52} d_3^2 \text{ cm}^{-3}$ , based on the normalization of model B in Table 1. With the estimated X-ray emitting volume  $V$  of  $37d_3^3 \text{ pc}^3$ , we arrive at  $n_e = 0.017(n_e/10n_{Fe})^{1/2} f^{-1/2} d_3^{-1/2} \text{ cm}^{-3}$ . The factor  $(n_e/10n_{Fe})^{1/2}$  is of the order of unity for a pure Fe plasma with  $\tau = 10^9 \text{ cm}^{-3} \text{ s}$ , but it is somewhat uncertain because of the poorly known electron distribution function and a possible contribution to  $n_e$  from other heavy elements which might be present in the ejecta. The electron distribution function may well be non-Maxwellian in such a low-density and high-temperature plasma because of the long Coulomb collision timescale. In particular, the distribution may be

bi-modal, with free preshock electrons heated to high temperatures at the collisionless shock, and with much colder electrons released in the process of collisional ionization in the postshock region (Hamilton & Sarazin 1984b). The electron density  $n_e$  just quoted refers to the hot component, and not to cold electrons with energies much below the Fe K-shell ionization threshold. For a pure Fe plasma with electron density  $0.017 \text{ cm}^{-3}$  and  $\tau = 10^9 \text{ cm}^{-3} \text{ s}$ , the plasma age is about 2000 yr, which is consistent with the relatively large age of RCW 86.

The presence of low-density Fe-rich ejecta in RCW 86 is consistent with the large observed equivalent widths of the Fe  $K\alpha$  line, which already led Bocchino et al. (2000) to suggest the possible presence of SN ejecta in this remnant. The morphology of synchrotron-emitting filaments apparently associated with the ejecta is also suggestive. The X-ray and radio synchrotron-emitting filaments are located mostly interior to the bright nonradiative and radiative shocks in the “knee” region of the remnant. These filaments form a ridge which extends much further to the east, and which is clearly located well within the blast wave outlined by nonradiative Balmer-emitting shocks (Smith 1997). The brightest part of this ridge is in the region of highest pressures where the most intense interaction of supernova ejecta with the ambient ISM is occurring, as judged by the presence of bright radiative and nonradiative shocks. This morphology is consistent with identification of this ridge with the reverse shock. In addition to solving the short timescale puzzle, the presence of low-density Fe-rich SN ejecta also removes a need for a mixed thermal-nonthermal continuum postulated by us previously for the synchrotron emission region (BRRD; see also Bamba, Koyama, & Tomida 2000). This required a coincidental match in intensities of synchrotron and thermal continuum emission in the 1–10 keV range. This is no longer necessary, since the observed continuum is mostly synchrotron emission, and the thermal contribution to the continuum may be as much as 2 or 3 orders of magnitude fainter.

### 4.3. X-Ray Synchrotron Spectra

No synchrotron component was required to obtain a reasonable fit for the soft region (Fig. 9); an upper limit to the rolloff frequency of about  $2 \times 10^{16}$  Hz was obtained as described in the previous section. We find values of  $\nu_{\text{rolloff}}$  of  $(7 - 10) \times 10^{16}$  Hz from the fits to hard regions, with remarkably little dispersion. These values are two to three times higher than those we reported in BRRD, for two reasons. First, the enormously improved spatial resolution of *Chandra* allows us to select spectral regions for extraction that are localized to the very hardest X-ray emission, whereas the fits based on ASCA data are necessarily averages over much larger regions, lowering the mean value of  $\nu_{\text{rolloff}}$ . Second, as described above, we now believe the entire hard continuum, rather than just part of it, to be due to synchrotron X-rays.

The values of  $\nu_{\text{rolloff}}$  can be understood in the framework of simple estimates of particle shock-acceleration times (see, for example, Reynolds 1998). If the maximum energy that electrons can reach is limited by radiative losses, the energy at which energy gains by acceleration equal losses due to radiation is about

$$E_m \sim 50 (\eta R_J)^{-1/2} (B_1/3 \mu\text{G})^{-1/2} u_8 \text{ ergs,}$$

where  $\eta$  is the ratio of electron mean free path to gyroradius (and is assumed constant),  $B_1$  is the upstream magnetic-field strength, and  $u_8$  is the shock speed in units of  $10^8 \text{ cm s}^{-1}$ . We have assumed a shock compression  $r$  of 4. The factor  $R_J$  is Jokipii's (1987) expression for the obliquity-dependence of the particle acceleration rate; where the shock is nearly perpendicular (i. e., the shock normal nearly perpendicular to the upstream magnetic field direction),

$$R_J \sim \left( \frac{2}{1+r} \right) (1 + \eta^2)^{-1}$$

so that for  $\eta$  substantially greater than 1,  $\eta R_J \propto \eta^{-1}$  and  $E_m \propto \eta^{+1/2}$ . Electrons of this

energy radiating in the downstream field  $B_2$  produce their peak power at a frequency

$$\nu_c \sim 5 \times 10^{16} (\eta R_J)^{-1} (B_2/4 B_1) u_8^2.$$

If reverse shock velocities are comparable to the blast-wave velocities of  $400 - 900 \text{ km s}^{-1}$ , then, we can reach the observed values of  $\nu_{\text{rolloff}}$  for compression ratios substantially larger than 4, and/or values of  $\eta$  substantially greater than 1. (Notice that the characteristic frequency radiated by electrons whose maximum energy is set by radiative losses is independent of the magnetic-field strength.) It should not be surprising that the hard emission is so restricted in spatial distribution, then; many of the shocks present in RCW 86 will not be fast enough to produce synchrotron X-ray-emitting electrons. Only in a few regions where the conditions are right will we expect such electrons to be accelerated.

We should add that the model we use to describe the synchrotron emission, *srcut*, is highly oversimplified: it is just the synchrotron emissivity of a power-law distribution of electrons with an exponential cutoff (the fastest plausible cutoff for shock-accelerated particles; see references in Reynolds & Keohane 1999), radiating in a uniform magnetic field. Much more elaborate models of spherical remnants in which radiative losses limit electron acceleration were described in Reynolds (1998); those models, not available in XSPEC, produced synchrotron spectra with a somewhat different shape than *srcut*. While the curvature within the *Chandra* bandpass is not enough to distinguish the difference, the inferred values of  $\nu_{\text{rolloff}}$  would probably be slightly different for a true loss-limited model. In fact, since any spatial inhomogeneities will broaden the cutoff, *srcut* represents the steepest possible cutoff of emission, and will give the highest rolloff frequency compatible with the observed data. Any more realistic model should produce a somewhat lower value.

Our fits to the synchrotron component could be substantially better constrained if radio fluxes were known more accurately. The most straightforward way to accomplish this would be to map RCW 86 with a large single dish, such as the Parkes telescope, and

combine those data with the ATCA interferometer image. This would allow considerably firmer determinations of  $\nu_{\text{rolloff}}$ .

We have argued that the hard continuum and Fe  $K\alpha$  line tend to be found together, strongly suggesting that it is the reverse shock that is responsible for accelerating particles to the highest energies. This conclusion is important to confirm, since it seems not to be obviously the case in other remnants with synchrotron X-ray emission. There is no obvious reason that reverse shocks should not be as effective as the blast wave at accelerating particles, for the same values of physical parameters such as shock speed and  $\eta$ . In RCW 86, blast-wave emission, while detectable, is so faint that synchrotron X-rays would be below the level of background, so we cannot rule out electron acceleration to comparably high energies at the blast wave.

Observing particle acceleration at the reverse shock may also have interesting consequences for the acceleration of cosmic rays. The direct acceleration of enriched material in supernova remnants might play a role in models of Galactic cosmic-ray acceleration and of chemical enrichment of the light elements Li, Be, B in the early Galaxy, when the carbon and oxygen from which these elements are spalled were less abundant in the general interstellar medium.

Even more intriguing is the possibility that the reason RCW 86 shows particular evidence for particle acceleration at the reverse shock is that the radiating particles are not electrons but positrons produced by decay of radioactive  $^{56}\text{Ni}$  synthesized in the explosion. A longstanding theoretical difficulty in electron acceleration has been the “injection problem”: thermal electrons have such small gyroradii that they see the shock as a smooth transition and not the discontinuity in flow speeds required for standard diffusive shock acceleration (see, e. g., Levinson 1992, 1994 for extensive discussion). Various suggestions have been made about how Nature evidently overcomes this difficulty. However, it has been

noted (Ramaty & Lingenfelter 1979; Ellison, Jones, & Ramaty 1989) that positrons released by radioactive decay of  $^{56}\text{Ni}$  and  $^{56}\text{Co}$  have typical energies of order 1 MeV, where they should see the shock as a discontinuity and be accelerated as efficiently as protons of similar energies. A reverse shock moving into Fe-rich ejecta should encounter a population of “pre-injected” energetic positrons which can be immediately accelerated efficiently. While this is a possibility difficult to rule out, we note that the decay lifetimes of  $^{56}\text{Ni}$  and  $^{56}\text{Co}$  are both less than a year; such positrons were almost entirely produced about  $10^4$  years ago, just after the supernova. Any X-ray-synchrotron-emitting positrons cannot have been accelerated soon after that, because the radiative lifetime is less than 1000 yr. However, 1 MeV positrons will lose energy primarily by adiabatic expansion losses, which could reduce them to no better than thermal electrons after  $10^4$  yr. This fascinating possibility must remain a speculation at this time.

## 5. CONCLUSIONS

The major conclusion of our paper is that the detailed morphology of soft and hard X-rays in RCW 86 strikingly supports the hypothesis of different origins. Our spectral analysis confirms that the hard X-rays are best described as a synchrotron continuum with Fe  $K\alpha$  emission that must come from a thermal component with a substantial overabundance of iron with respect to solar. This result implies that some of the original supernova ejecta are still unmixed after  $\sim 10^4$  yr, and that the reverse shock into those ejecta can also accelerate electrons to X-ray synchrotron-emitting energies of order 50 TeV.

Both these conclusions substantially complicate the task of understanding the X-ray spectra of middle-aged supernova remnants. Apparently even after ages of order  $10^4$  years, remnants are not in the simple Sedov phase, and the possibility of synchrotron X-ray emission confusing the analysis of thermal emission cannot be neglected. The only ultimate

solution to this problem requires X-ray spectroscopy with much higher energy resolution. (Grating resolution is adequate, but grating observations of large extended sources with *Chandra* or *XMM-Newton* are virtually uninterpretable.) The *Astro-E2* microcalorimeters hold out the possibility of spatially resolved spectroscopy with enough resolution to allow the inference of temperatures from line complexes alone without requiring any assumptions about the continuum. In that case, one can immediately determine the extent of synchrotron contributions to the continuum.

With *Chandra's* spatial resolution, we can for the first time discern discrete shock features and minimize projection effects, which should aid substantially in the detailed thermal modeling that will be the next step in understanding RCW 86. The hard X-ray emission appears to delineate particular shocks, where both radio and X-ray emitting electrons are accelerated. The greater extent of radio emission behind such features is expected from preferential energy losses on the much more energetic X-ray emitting electrons. The width of the X-ray emission is quite consistent with this interpretation, for expected post-shock velocities of hundreds of  $\text{km s}^{-1}$  and magnetic field strengths of order  $10 \mu\text{Gauss}$ .

The observed rolloff frequencies in areas containing synchrotron continua can be understood in terms of radiative-loss-limited shock acceleration, but simple estimates require favorable conditions to reach the inferred electron energies. In particular, nearly perpendicular shocks reach higher energies more readily, and this may be one factor that distinguishes shocks that produce synchrotron X-ray continua from those which do not. We repeat, however, that the *srgut* model is highly simplified, and fits with more elaborate models might produce somewhat different values for  $\nu_{\text{rolloff}}$ .

Progress in understanding RCW 86, and the general problems it raises for the understanding of supernova remnants, requires further observations in various bands.

*XMM-Newton* observations can obtain significantly higher signal-to-noise ratios at high energies, allowing testing in other regions of our claim of an association of Fe  $K\alpha$  emission with regions of hard continuum. Optical and infrared observations in principle should be able to detect synchrotron continuum at a level exactly predictable from our fits, but distinguishing it from the confusing emission might prove extremely challenging. Since our fitted values of  $\nu_{\text{rolloff}}$  are far above optical frequencies, we expect that there should be little difference between the optical or IR morphology of synchrotron emission and the radio morphology. A strategy to search for extremely faint diffuse emission then might center on sharp features in the radio image, such as the edge coincident with a hard X-ray filament in the middle of chip S3.

Support for this work was provided by NASA through *Chandra* grant G01-2077A and G01-2077B. J. R. acknowledge the support of California Institute of Technology, the Jet Propulsion Laboratory, which is operated under contract with NASA. We thank Sara Gallagher and Leisa Townsley for help with CTI correction of *Chandra* RCW 86 data, John Dickel for making Australia Telescope radio data available to us, and Chris Smith for his RCW 86  $H\alpha$  image. We acknowledge discussions with Don Ellison about particle acceleration in reverse shocks, including acceleration of positrons produced in radioactive decays.

## A. Appendix

Here we demonstrate that nonthermal bremsstrahlung is unlikely to be important in the regions we have analyzed in RCW 86. First, we shall show that such an explanation for the lower-energy continuum would require a huge unseen cold-electron population of which the observed  $\sim 2$  keV electrons are the tail. The short timescale for Coulomb equilibration

of these  $\sim 2$  keV electrons with the cold population would require that the cold population have an enormous density; it would itself cool rapidly and produce copious unseen optical emission, and the energy required to maintain the warmer population would be exorbitant. We then show that even the  $\sim 5$  keV continuum near the Fe  $K\alpha$  line is unlikely to be nonthermal bremsstrahlung. Again, the energetics of maintaining the hot population against energy transfer into the cold population would require that a significant portion of the blast energy go into electrons with energies of order 5 keV, which seems unreasonable.

We showed in §4.2 that the Fe  $K\alpha$  line cannot be produced in a thermal plasma with approximately solar abundances. Is it possible to account for the observed Fe  $K\alpha$  emission by postulating deviations from a Maxwellian electron distribution in such plasma, as suggested by Vink et al. (1997, 2002)? First we consider whether the featureless spectrum at lower energies ( $\sim 2$  keV), which we interpret as nonthermal synchrotron emission, could be attributed to nonthermal bremsstrahlung produced by suprathermal electrons accelerated in the shock wave. The following arguments based on order-of-magnitude estimates demonstrate that this is not possible. For the nonthermal bremsstrahlung hypothesis, one needs a large thermal pool of cold electrons with temperature  $T_c$ , and much less numerous suprathermal electrons forming a power-law tail at high electron energies. The description of these fast electrons in terms of a power law is a crude approximation because of Coulomb losses to the cold electrons, and because the particle acceleration process at the shock may produce a curved (concave) spectrum instead of a power law (Ellison & Reynolds 1991; Reynolds & Ellison 1992). In view of these complexities, we do not attempt to model the electron distribution function, but assume instead a Maxwellian distribution of hot electrons. Such a two-component (cold+hot) thermal model is sufficient for our present purpose of estimating the number density of fast electrons which would be required to account for the observed strength of the featureless X-ray continuum. The bulk plasma temperature  $T_c$  must be low enough that the ionization state of the gas is so low that

practically no X-ray lines are produced in the *Chandra* energy range, to be consistent with the observed featureless spectra. The observed X-ray continuum would then be free-free emission produced by fast electrons in collisions with protons and  $\alpha$  particles. In order to estimate the required density of fast electrons, we fit a standard free-free emission model to the spectrum shown in Figure 10. We obtain a hot electron temperature  $T_h$  of 1.45 keV, and corresponding emission measure  $EM_h = \int n_{eh}n_H dV$  of  $2.6 \times 10^{57} d_3^2 \text{ cm}^{-3}$  (where  $n_{eh}$  is the number density of hot electrons, which must be much smaller than the hydrogen density  $n_H$ ). For the X-ray emitting volume of  $37 d_3^3 \text{ pc}^3$  estimated in §4.2,  $n_{eh} = 2.4/f_h n_H d_3 \text{ cm}^{-3}$ , where  $f_h$  is the unknown volume filling fraction of fast electrons.

The hot electron temperature of 1.45 keV implies an average energy  $E$  for fast electrons of 2.2 keV. Electrons with such a low energy lose it rapidly in Coulomb collisions with cold electrons in the thermal pool. The Coulomb energy loss timescale  $t_E$  is equal to  $32E^{3/2}/G((E/T_c)^{1/2})n_e \ln \Lambda \text{ yr}$  (Spitzer 1962), where  $n_e = 1.2n_H$  is the density of cold electrons,  $\ln \Lambda$  is the Coulomb logarithm, and the function  $G$  is tabulated by Spitzer (1962). Because expected electron densities are high ( $n_e \gg 1 \text{ cm}^{-3}$ ), this is a short time scale. For example, for  $E = 2.2 \text{ keV}$  and  $T_c = 0.1 \text{ keV}$ , we find  $\ln \Lambda = 30$ ,  $(E/T_c)^{1/2} = 4.7$ ,  $G(4.7) = 0.024$ , and  $t_E = 140n_e^{-1} \text{ yr}$ . This short Coulomb energy exchange time  $t_E$  implies that 2 keV electrons are strongly coupled to the low-temperature thermal plasma through Coulomb collisions. This strong thermal coupling demands that the thermal energy in fast electrons be much smaller than in the cold thermal pool, otherwise the energy so quickly transferred to the cold electrons would raise their temperature enough to produce strong X-ray lines, contrary to observations.

Let  $R \equiv (n_e + n_H)T_c/n_{eh}T_h$  denote the cold/hot energy ratio, which we demand to be much larger than unity. Using our estimates for  $n_{eh}$  obtained above from the strength of the X-ray continuum,  $R = 0.62f_h n_e^2 d_3 T_c/T_h$ . Because of the strong coupling through

Coulomb collisions, the volume filling fraction  $f_h$  is expected to be low for shock-accelerated fast electrons, on the order of  $t_E/t_s$  or less, where  $t_s$  is the shock age. The expected shock age  $t_s$  should be a sizeable fraction of the remnant's age, which is  $\sim 10^4 d_3$  yr (Rosado et al. 1996). Denoting  $t_{s,4} = t_s/10^4$  yr and using the expression for  $t_E$  obtained above, we arrive at  $R = 0.002 E^{1/2} T_c n_e / t_{s,4} G((E/T_c)^{1/2}) \ln \Lambda$ . By equating  $R$  to 1, we obtain a conservative lower limit to the cold electron density  $n_e$  of  $500 t_{s,4} G((E/T_c)^{1/2}) \ln \Lambda E^{-1/2} T_c^{-1} \text{ cm}^{-3}$ . This is a very large electron density, e. g., even for a relatively recent ( $t_{s,4} = 0.2$ ) shock with  $E = 2.2$  keV, and  $T_c$  in the range of 0.05–0.1 keV, we arrive at  $n_e \sim 500 \text{ cm}^{-3}$ . Even if  $T_c < 0.1$  keV, the density of this cold plasma is large enough to produce a significant amount of very soft X-ray emission which would be easily seen in X-ray spectra. In addition, such plasma is located close to the peak of the cooling function, and it would itself cool and recombine on timescales much smaller than the age of the remnant even in the presence of magnetic pressure support. Such a cooling and recombining plasma should produce strong optical emission. There is no evidence for optical emission at the location of the hard X-ray emitting filaments in the optical images presented by Smith (1997). Another problem is the high ( $6.5 \times 10^{-8} \text{ dynes cm}^{-2}$ ) pressure of hot electrons, which exceeds the estimated ram pressure of the blast wave by an order of magnitude or more. This problem becomes more acute if the filling fraction  $f_h$  is not small. In this case one must assume that an additional energy source exists throughout the X-ray emitting plasma, which could heat hot electrons and balance their Coulomb losses. The power required to achieve this balance far outstrips the amount of kinetic energy in the blast wave. We conclude that the observed X-ray continuum emission at low energies cannot be produced by nonthermal bremsstrahlung.

While the low-energy continuum is almost certainly synchrotron radiation, the high-energy continuum in the vicinity of the Fe  $K\alpha$  line could in principle be produced by nonthermal bremsstrahlung by high energy suprathermal electrons. Because of the high ( $\sim 5 - 10$  keV) electron energies required to produce this continuum, such electrons

will be less strongly coupled to the cold electrons through Coulomb collisions than the  $\sim 2$  keV electrons considered above. The high energy continuum is nevertheless quite strong, implying a high density  $n_{eh}$  for these fast electrons and nonnegligible thermal coupling between cold and fast electrons. We can repeat our previous arguments where now the subscript  $h$  refers to the  $\sim 5 - 10$  keV electrons. Using our thermal fit to the high energy continuum and our estimates of the X-ray emitting volume (see §4.2), we arrive at  $n_{eh} = 0.48/f_h n_H d_3 \text{ cm}^{-3}$ . Next, we estimate the energy transfer rate from hot to cold electrons, again approximating their electron distribution functions by Maxwellians with low ( $T_c$ ) and high ( $T_h$ ) temperatures. This rate (per unit volume) is equal to  $-\frac{3}{2}n_{eh}kdT_h/dt = \frac{3}{2}n_{eh}k(T_h - T_c)/t_{eq}$ , where  $t_{eq}$  is the equipartition time between two Maxwellian electron distributions given by Spitzer (1962). With our estimate for  $n_{eh}$ , and assuming that  $T_c \ll T_h$ , we arrive at the energy transfer rate of  $0.86kT_h/n_e t_{eq} f_h d_3$ . Note that because  $t_{eq} \propto n_e^{-1}$ , this energy transfer rate is independent of the density of cold electrons. For  $kT_h = 5$  keV,  $f_h = 1$ , we arrive at a conservative lower limit to the energy transfer rate of  $3.4 \times 10^{-18} d_3^{-1} \text{ ergs cm}^{-3} \text{ s}^{-1}$ . If we now neglect fast electron energy losses, i. e., if we assume that  $T_h$  is constant so that the fast electrons coexist with the cold electrons throughout the whole X-ray emitting plasma, we find that in 1,000 yr the total amount of transferred energy is equal to  $1.1 \times 10^{-7} \text{ ergs cm}^{-3}$ . This would result in a thermal pressure of the cold plasma of  $7.1 \times 10^{-8} \text{ dynes cm}^{-3}$ , more than the ram pressure of the blast wave, where velocities range up to  $900 \text{ km s}^{-1}$  and preshock densities may be as high as  $\sim 1 \text{ cm}^{-3}$  (Ghavamian et al. 2001). While there are some uncertainties in estimates of the preshock density because of the unknown preshock ionization fraction, this finding suggests that  $\sim 5 - 10$  keV electrons would play a major role in the energy balance of the plasma. This is not expected in standard particle acceleration models where most of the shock kinetic energy is transferred to cosmic-ray particles, and would rule out the simultaneous production of  $\sim 100$  times as much energy in accelerated ions, as observed in

cosmic rays at Earth.

This problem remains if we relax our assumption of constant  $T_h$  by allowing for Coulomb energy losses. We assume that fast electrons are injected at the shock front with energy  $E$  and then lose their energy on a timescale  $t_E = 5.3 \times 10^3 n_e^{-1}$  yr ( $t_E$  was estimated here in the limit of  $T_c = 0$ ). For expected electron densities  $n_e$  far in excess of  $1 \text{ cm}^{-3}$ , Coulomb energy losses are important. The volume filling fraction  $f_h$  for plasma containing fast electrons is then small, less than  $\sim t_E/t_s = 0.53 t_{s,4}^{-1} n_e^{-1}$ . With this volume fraction, we arrive at  $n_{eh} = 1.6 t_{s,4} \text{ cm}^{-3}$ , and with  $T_h = 5 \text{ keV}$  the pressure of fast electrons is equal to  $2.6 \times 10^{-9} \text{ dynes cm}^{-2}$  even for a relatively young ( $t_{s,4} = 0.2$ ) shock. This pressure is substantial when compared with the estimated ram pressure, again implying a major role in the plasma energetics for  $\sim 5 - 10 \text{ keV}$  electrons. It is hard to explain this in the framework of our current understanding of collisionless plasmas and the particle acceleration process. While we cannot completely rule out nonthermal bremsstrahlung as the explanation for the high-energy continuum on an observational basis alone, we do not favor it because of excessive energy requirements.

Table 1. Spectral Models

Model Parameters	Soft Region		Hard Region (S3)		Hard Filaments (S3)		I3 Filament
	A <sup>a</sup>	B <sup>b</sup>	A	B	A	B	A
$N_H/10^{21} \text{ cm}^{-2}$	$5.88^{+0.03}_{-0.06}$	$5.26^{+0.16}_{-0.16}$	$4.43^{+0.14}_{-0.14}$	$4.16^{+0.10}_{-0.11}$	$4.94^{+0.35}_{-0.34}$	$4.61^{+0.41}_{-0.30}$	$3.80^{+0.37}_{-0.40}$
$kT$ (keV)	$0.415^{+0.015}_{-0.008}$	$0.430^{+0.015}_{-0.017}$	$0.675^{+0.052}_{-0.057}$	$0.675^{+0.025}_{-0.101}$	$0.60^{+0.22}_{-0.17}$	$0.48^{+0.27}_{-0.13}$	$2.1^{+1.5}_{-1.1}$
$\tau/10^{10} \text{ cm}^{-3}\text{s}$	$2.77^{+0.10}_{-0.12}$	$5.09^{+0.67}_{-0.50}$	$1.74^{+0.18}_{-0.17}$	$2.34^{+0.77}_{-0.24}$	$1.71^{+0.96}_{-0.45}$	$3.88^{+5.16}_{-1.76}$	$2.20^{+2.59}_{-0.53}$
C, N	$1.20^{+0.07}_{-0.08}$	$0.80^{+0.18}_{-0.17}$	1	0.80	1	0.80	1
O	$1.20^{+0.07}_{-0.08}$	$0.86^{+0.11}_{-0.10}$	1	0.86	1	0.86	1
Ne	$1.20^{+0.07}_{-0.08}$	$0.99^{+0.09}_{-0.09}$	1	0.99	1	0.99	1
Mg	$1.20^{+0.07}_{-0.08}$	$0.67^{+0.06}_{-0.07}$	1	0.67	1	0.67	1
Si	$1.20^{+0.07}_{-0.08}$	$0.92^{+0.09}_{-0.08}$	1	0.92	1	0.92	1
S	$1.20^{+0.07}_{-0.08}$	$0.85^{+0.19}_{-0.19}$	1	0.85	1	0.85	1
Fe, Ni, Ca	$1.20^{+0.07}_{-0.08}$	$0.63^{+0.06}_{-0.06}$	1	0.63	1	0.63	1
$(EM/4\pi d^2)/10^{11} \text{ cm}^{-5}$	$23.2^{+1.7}_{-1.7}$	$20.5^{+1.8}_{-1.8}$	$1.90^{+0.28}_{-0.30}$	$1.79^{+0.29}_{-0.20}$	$0.47^{+0.33}_{-0.16}$	$0.50^{+0.54}_{-0.20}$	$0.12^{+0.05}_{-0.03}$
$kT_{ej}$ (keV)			5	5	5	5	
$\tau_{ej}$ (cm <sup>-3</sup> s)			10 <sup>9</sup>	10 <sup>9</sup>	10 <sup>9</sup>	10 <sup>9</sup>	
Fe K $\alpha$ EW (keV)			$0.38^{+0.13}_{-0.13}$	$0.37^{+0.13}_{-0.13}$	$0.17^{+0.17}_{-0.17}$	$0.16^{+0.18}_{-0.16}$	
$(EM_{ej}/4\pi d^2)/10^7 \text{ cm}^{-5}$			$2.91^{+0.99}_{-0.99}$	$2.88^{+0.99}_{-0.99}$	$0.26^{+0.26}_{-0.26}$	$0.24^{+0.27}_{-0.24}$	
$\nu_c/10^{16} \text{ Hz}$			$8.08^{+0.51}_{-0.51}$	$8.58^{+0.40}_{-0.44}$	$7.68^{+1.10}_{-1.03}$	$8.19^{+0.89}_{-1.47}$	$10.1^{+2.0}_{-1.4}$
$\alpha$			0.6	0.6	0.6	0.6	0.6
$F_{1\text{GHz}}$ (Jy)			$2.80^{+0.17}_{-0.17}$	$2.59^{+0.15}_{-0.11}$	$0.61^{+0.09}_{-0.08}$	$0.57^{+0.11}_{-0.06}$	$0.48^{+0.07}_{-0.08}$
X <sup>c</sup> (0.5-10 keV)	0%	0%	83%	84%	86%	88%	86%
Reduced $\chi^2$	5.87	2.69	1.43	1.39	1.05	1.03	1.16
Counts/s (0.5-10 keV)	2.5	2.5	2.0	2.0	0.37	0.37	0.27

<sup>a</sup>*pshock*

<sup>b</sup>*vpshock*

<sup>c</sup>Nonthermal/(nonthermal+thermal) flux ratio

## REFERENCES

- Allen, G. E., Gotthelf, E. V., & Petre, R. 1999, in the Proceedings of the 26th International Cosmic Ray Conference, Salt Lake City
- Arnaud, K. A. 1996, in *Astronomical Data Analysis and Systems V*, eds. G. Jacoby & J. Barnes, ASP Conf. Series, v.101, 17
- Bamba, A., Koyama, K., & Tomida, H. 2000, PASJ, 52, 1157
- Bamba, A., Ueno, M., Koyama, K., & Yamauchi, S. 2001, PASJ, 53, L21
- Bocchino, F., Vink, J., Favata, F., Maggio, A., & Sciortino, S. 2000, A&A, 360, 671
- Borkowski, K. J., Lyerly, W. J., & Reynolds, S. P. 2001, ApJ, 548, 820
- Borkowski, K. J., Rho, J., Reynolds, S. P., & Dyer, K. K. 2001, ApJ, 550, 334
- Brickhouse, N. S., Dupree, A. K., Edgar, R. J., Liedahl, D. A., Drake, S. A., White, N. E., & Singh, K. P. 2000, ApJ, 530, 387
- Dickel, J. R., Strom, R. G., & Milne, D. K. 2001, ApJ, 546, 447
- Dyer, K. K., Reynolds, S. P., Borkowski, K. J., Allen, G. E., & Petre, R. 2001, ApJ, 551, 439
- Ellison, D., Jones, C. F., & Ramaty, R. 1989, 21st International Cosmic Ray Conference, 4, 68
- Ellison, D., & Reynolds, S. P. 1991, ApJ, 382, 242
- Garmire, G. P., et al. 1992, in Proc AIAA, Space Programs and Technologies Conference
- Ghavamian, P., Raymond, J., Smith, R. C., & Hartigan, P. 2001, ApJ, 547, 995

- Green, D. A. 2001, A Catalogue of Galactic Supernova Remnants (2001 December version),  
Mullard Radio Astronomy Observatory, Cavendish Laboratory, Cambridge, United  
Kingdom
- Hamilton, A. J. S., & Sarazin, C. L. 1984a, ApJ, 284, 601
- Hamilton, A. J. S., & Sarazin, C. L. 1984b, ApJ, 287, 282
- Hamilton, A. J. S., & Sarazin, C. L., & Szymkowiak, A. E. 1986, ApJ, 300, 698
- Jokipii, J. R. 1987, ApJ, 313, 842
- Koyama, K., et al. 1997, PASJ, 49, L7
- Koyama, K., Petre, R., Gotthelf, E. V., Hwang, U., Matsuura, M., Ozaki, M., & Holt, S. S.  
1995, Nature 378, 255
- Laming, J. M. 1998, ApJ, 499, 309
- Levinson, A. 1992, ApJ, 401, L73
- Levinson, A. 1994, ApJ, 426, L327
- Liedahl, D. A., Osterheld, A. L., & Goldstein, W. H. 1995, ApJ, 438, L115
- Long, K. S., & Blair, W. P. 1990, ApJ, 358, L13
- Ramaty, R., & Lingenfelter, R.E. 1979, 16th International Cosmic Ray Conference, 1, 501
- Reynolds, S. P. 1998, ApJ, 493, 375
- Reynolds, S. P., & Ellison, D. 1992, ApJ, 399, L75
- Reynolds, S.P., & Keohane, J. W. 1999, ApJ, 525, 368
- Rosado, M., Ambrocio-Cruz, P., Le Coarer, E., & Marcelin, M. 1996, A&A, 315, 243

- Slane, P. , Gaensler, B. M., Dame, T. M., Hughes, J. P., Plucinsky, P. P. & Green, A. 1999, ApJ, 525, 357
- Slane, P., et al. 2001, ApJ, 548, 814
- Smith, R. C. 1997, AJ, 114, 2664
- Spitzer, L. 1962, *Physics of Fully Ionized Gases* (New York: Wiley)
- Townsley, L. K., Broos, P. S., Garmire, G. P., & Nousek, J. A. 2000, ApJ, 534, L139
- Vink, J., Bleeker, J. A. M., Kaastra, J. S., van der Heyden, K. J., Rasmussen, A. P., & Dickel, J. R. 2002, in *New Visions of the X-ray Universe in the XMM-Newton and Chandra Era*, ESTEC, in press
- Vink, J., Kaastra, J. S., & Bleeker, J. A. M. 1997, A&A, 328, 628
- Weisskopf, M. C., O'dell, S. L., & van Speybroeck, L. P. 1996, Proc. SPIE, 2805, 2
- Whiteoak, J. B. Z., & Green, A. J. 1996, A&AS, 118, 329

Fig. 1.— Total energy band (0.5–8 keV) *Chandra* image of RCW 86. The scale ranges from  $6 \times 10^{-8}$  to  $1 \times 10^{-6}$  photons  $\text{cm}^{-2} \text{s}^{-1} \text{arcsec}^{-2}$ . The two chips in the left column are, from top (north) down, I2 and I3; in the right column, S0, S1, S2, and S3. This and following images have been binned to a resolution of  $2''$ .

Fig. 2.— Mosaiced three-color *Chandra* images of RCW 86: red represents 0.5–1 keV photons; green, 1–2 keV; and blue 2–8 keV.

Fig. 3.— Soft (0.5–1 keV) X-ray image of RCW 86.

Fig. 4.— Hard (2–10 keV) X-ray image of RCW 86.

Fig. 5.—  $\text{H}\alpha$  image from Smith (1997) (in green) compared with the soft (0.5–1 keV) X-ray image (in red).

Fig. 6.— The 1.4 GHz ATCA image (Dickel et al. 2001) (in red) compared with hard (2–10 keV) and soft (0.5–1 keV) *Chandra* images (in blue and green, respectively).

The radio image has been smoothed to a resolution of  $8''$ .

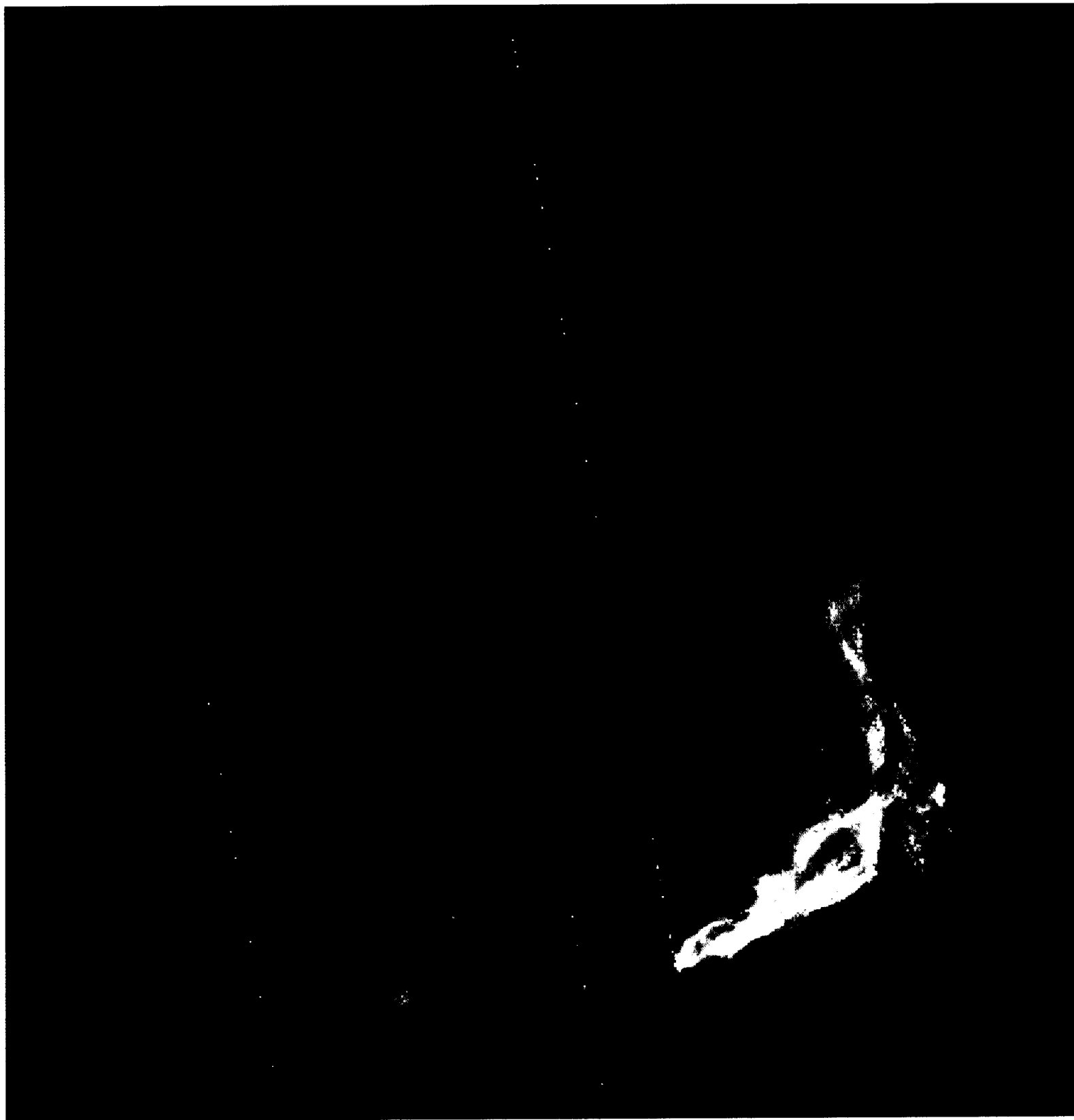
Fig. 7.— *Chandra* image in the 0.5–8 keV energy band with spectral extraction regions and spatial profiles indicated (in red and yellow, respectively).

Fig. 8.— Spatial profiles of hard (2–8 keV) X-ray emission and 1.4 GHz radio emission (*solid* and *dashed* lines, respectively) for three positions shown in Figure 7, from west (*top*) to east (*bottom*). X-ray emission is scaled independently for each profile relative to radio emission. Distance is measured in arcseconds, from E to W (*top* profile), and from NE to SW (*middle* and *bottom* profiles).

Fig. 9.— ACIS S3 X-ray spectrum of the bright nonradiative Balmer filament. Plane-parallel shock model (model B from Table 1) is shown by *solid line*.

Fig. 10.— ACIS S3 X-ray spectrum of the entire synchrotron-emitting region. Model B from Table 1 is shown by *solid line*. Individual models components are also shown: *srcut* – *short-dashed line*, pure Fe *vpshock* model – *long-dashed*, low-temperature *vpshock* model – *dash-dotted*.

Fig. 11.— ACIS S3 (top) and I3 (bottom) X-ray spectra of synchrotron-emitting filaments, with best-fit models from Table 1 shown by *solid lines*. Individual model components are also shown.





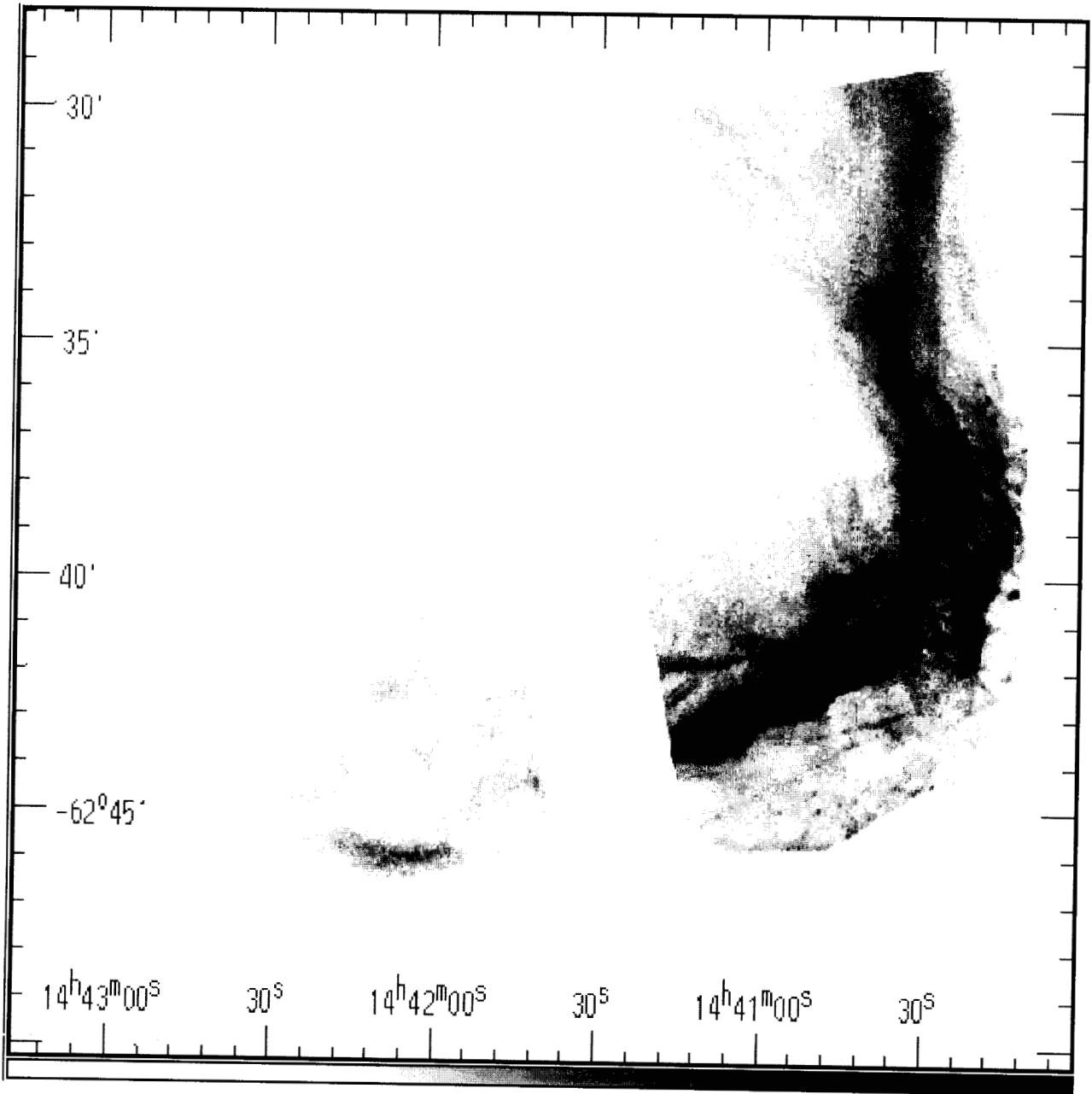


Fig. 3

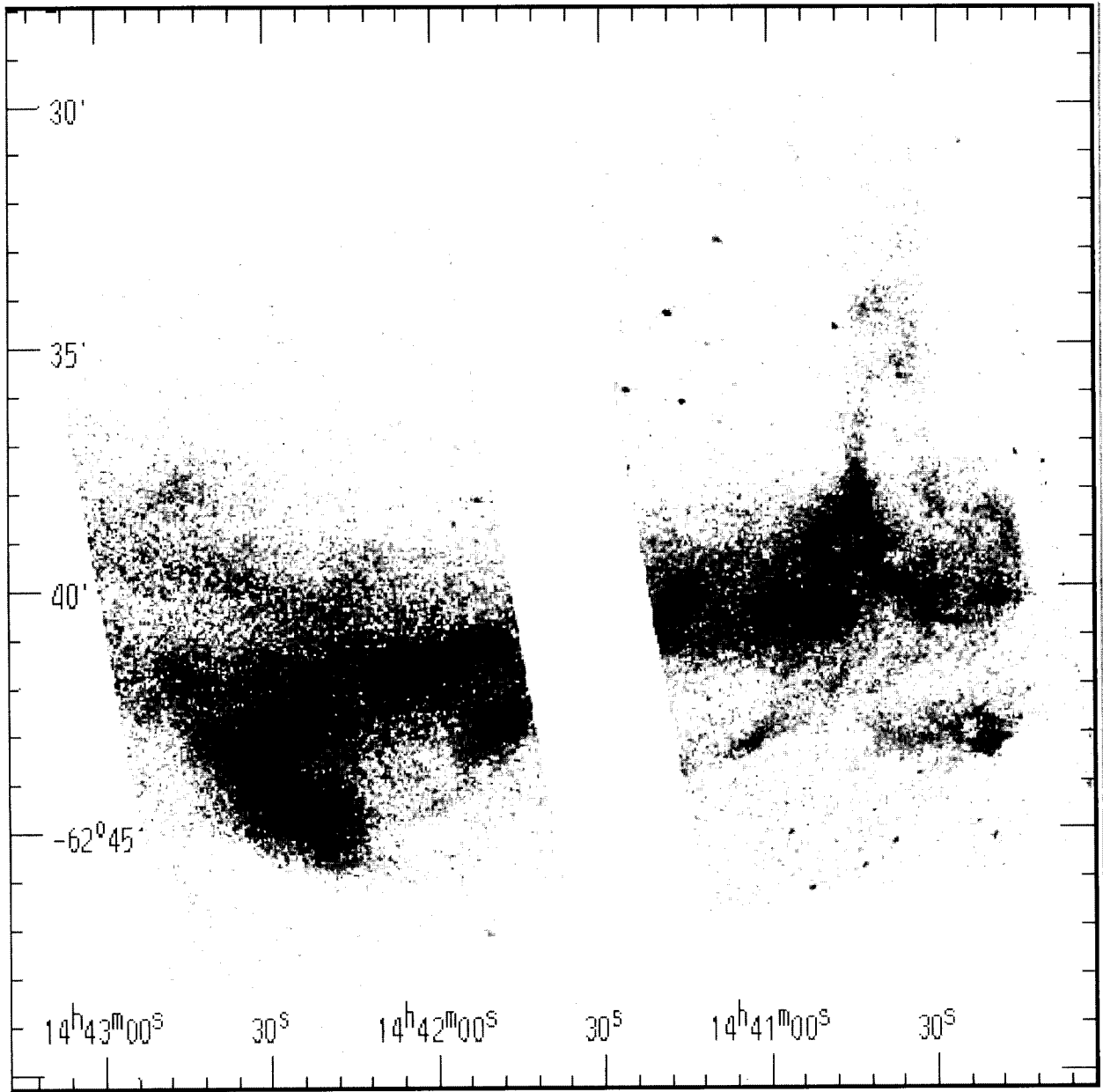
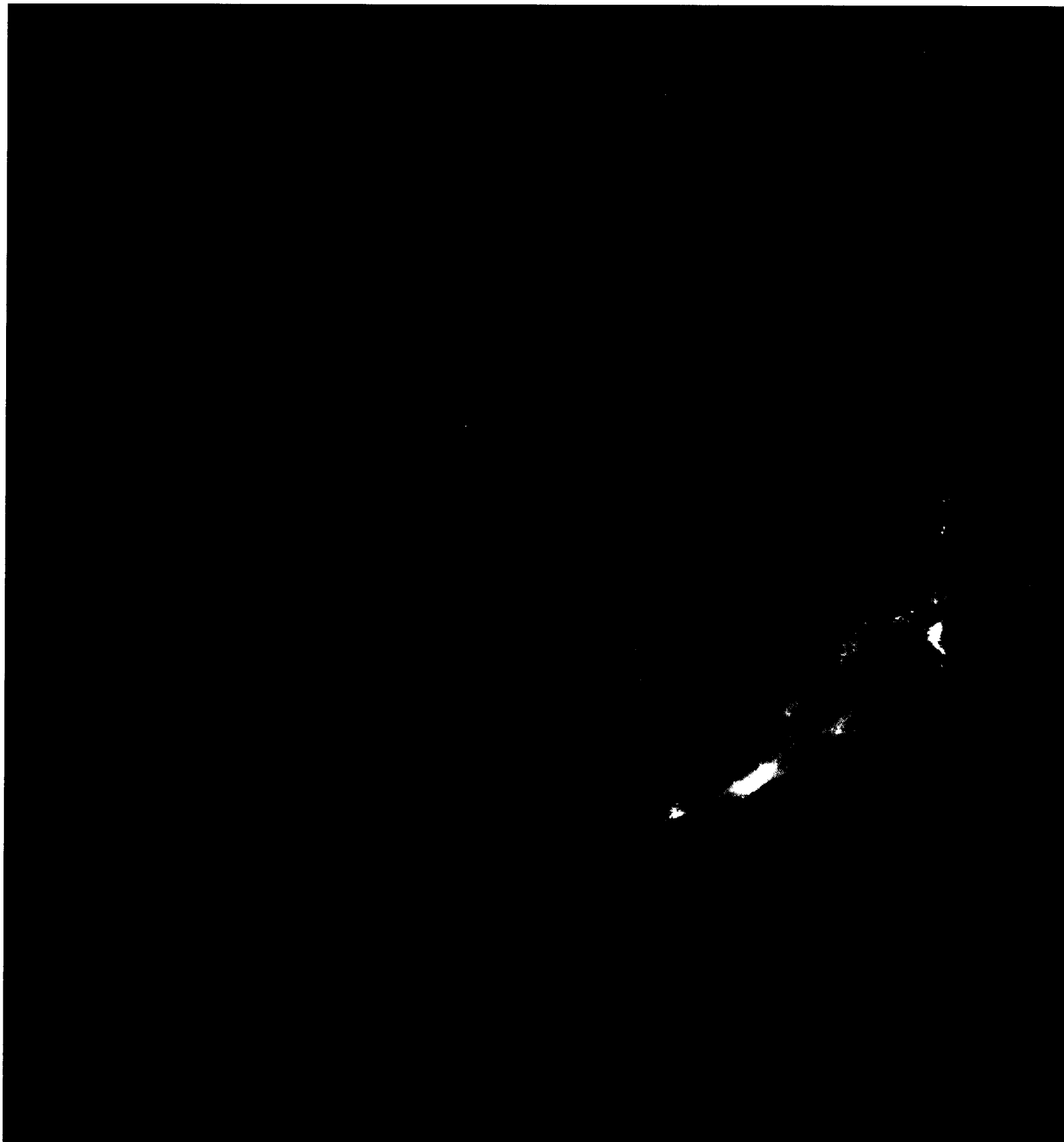


Fig. 4





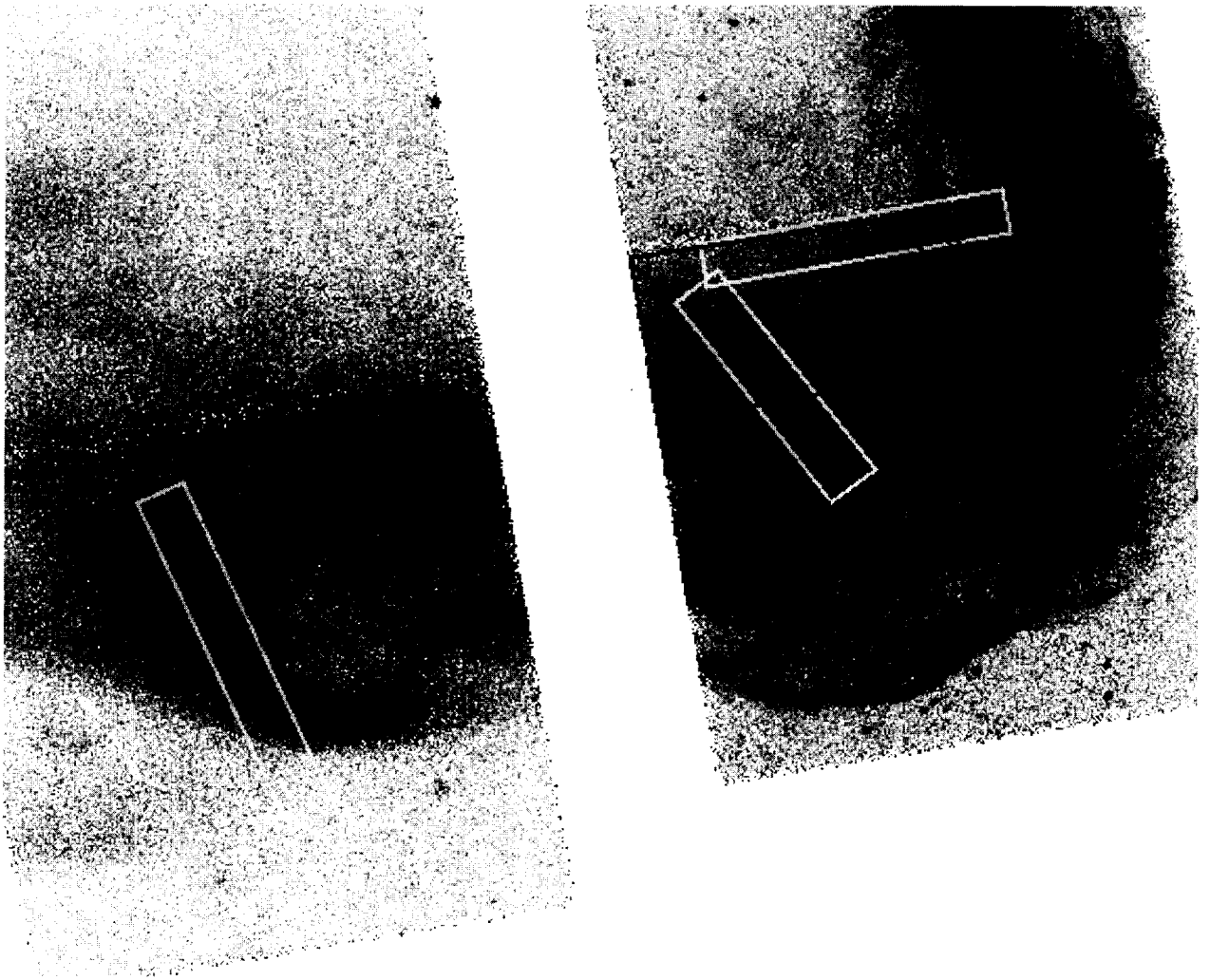


Fig. 7

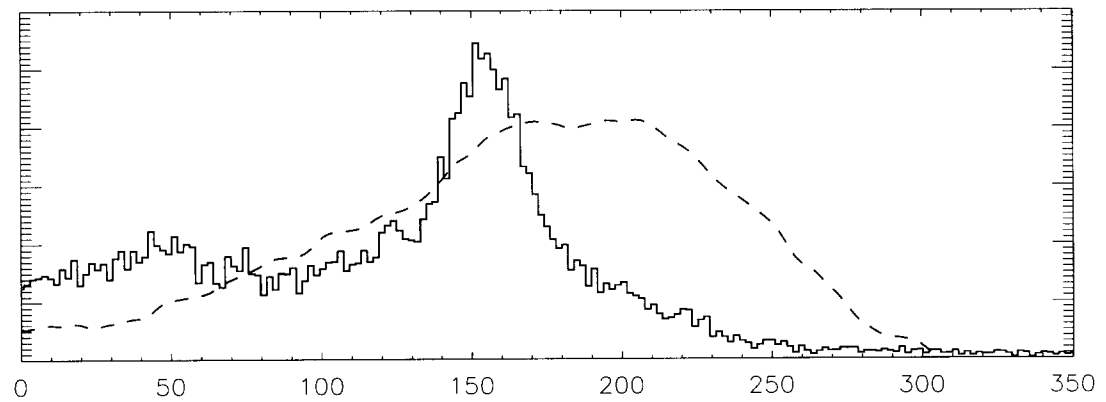
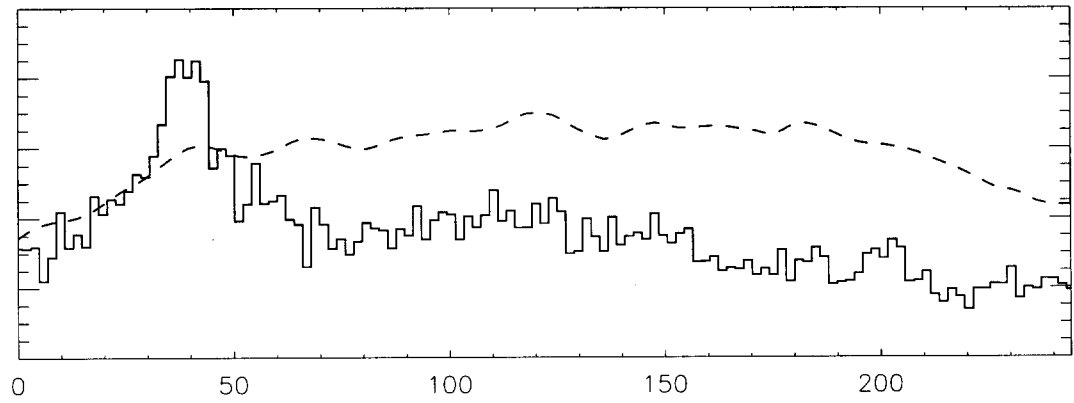
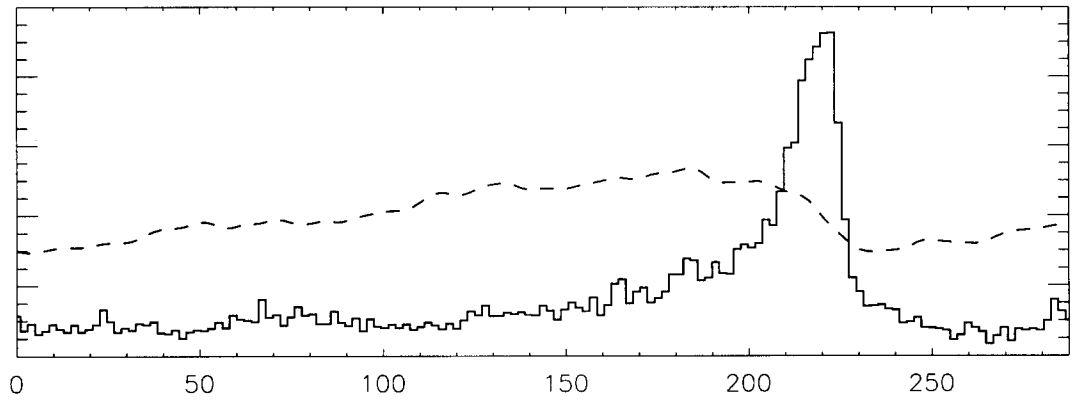


Fig. 8

